Free Surface Flow in High Speed Fiber Drawing With Large-Diameter Glass Preforms

Zhiyong Wei
e-mail: gte384w@prism.gatech.edu

Kok-Meng Lee*
e-mail: kokmeng.lee@me.gatech.edu

The George W. Woodruff School of Mechanical Engineering, Georgia Institute of Technology, Atlanta, GA 30332-0405

Serge W. Tchikanda
Sandia National Laboratories, MS 9161, 7011 East Ave, Livermore, CA 94550

Zhi Zhou
e-mail: zhizhou@ofsoptics.com

Siu-Ping Hong
e-mail: shong@ofsoptics.com

OFS, Norcross, GA 30071

This paper presents a complete two-dimensional (2D) thermofluid model for predicting the neck-down shape in the fiber drawing process. This model uses the controlled draw tension to calculate the Neumann boundary condition at the furnace exit; thus, it does not require specifying the speed (or diameter) of the fiber as most previous studies did. The model presented here can be applied to optimization of the high-speed draw process with large-diameter preforms. In this study, the radiative transfer equation is directly solved for the radiation fluxes using the discrete ordinate method coupled with the solution of the free surface flow, which does not assume that the glass is optically thick and does not neglect the glass absorption at the short-wavelength band. The artificial compressibility method is used to solve the Navier-Stokes equations. A staggered-grid computation scheme that is shown to be efficient and robust was used to reduce the computation load in solving the complete 2D model. The neck-down profile of a large preform (9 cm dia) drawn at a relatively high speed of 25 m/s was experimentally measured. The measured profile well matches that derived numerically. Results also show that the free surface calculated using the Dirichlet boundary condition deviates considerably from the measured profile, particularly near the furnace exit where the actual diameter (and, hence, the speed of the glass) is essentially unknown. Although the difference between the numerical results obtained from the full and semi-2D models was small, this difference could be significant if the location at which the glass converges to 125 μm dia is of interest, especially when the preform has a large diameter drawn at a high speed.
[DOI: 10.1115/1.1795237]

1 Introduction

A number of industrial processes, such as Czochralski crystal growth, VAD preform stretching, and optical fiber drawing, involve free surface flow coupled with complex radiative transfer in semitransparent materials. In manufacturing optical fibers, difficulties in making practical measurements in the furnace domain of the drawing process have motivated manufacturers to look for numerical tools to facilitate the design of new processes for drawing optical fibers at high speed from large-diameter preforms (glass rod). Significant efforts have been directed toward the modeling of a fiber-drawing process for the past three decades. Most of the existing models assume a Dirichlet boundary condition (DBC) at the furnace exit. This formulation is valid for drawing small-diameter preform as long as the glass fiber solidifies within the furnace. As larger preforms are drawn at higher speeds, the fiber diameter (or speed) at the furnace exit is essentially unknown because the glass often freezes into fiber well outside the furnace.

An accurate analytical prediction of the free surface being drawn is challenging in that the momentum and energy equations characterizing the drawing process are strongly coupled and nonlinear due to the highly temperature-dependent viscosity of the glass and the effects of the radiative heat transfer. During the late 1970s and the 1980s, various aspects of the optical fiber-draw problems were studied by a number of researchers, which include Paek and Runk [1], Homsy and Walker [2], Myers [3], and Vasiljev et al. [4]. These studies primarily focused on one-dimensional (1D) models for drawing fibers from small-diameter preforms at a relatively slow speed.

Radiative transfer is the dominant mode of heat transfer in the fiber-draw process. In [2], it was found that the Rosseland diffu-

sion (optically thick medium) assumption would fail at the surface—an assumption commonly used in many early studies due to its simplicity in solving the radiative transfer in the semitransparent glass. Wei et al. [5] confirmed this finding in a study of radiative transfer modeling on a moving glass rod. They also numerically solved the radiative transfer equation (RTE) using the discrete ordinate method (DOM) to predict the temperature gradient built up during transient. In addition, their analysis showed that the glass absorption coefficient in the short-wavelength band cannot be neglected and proposed a modified band model that includes the glass absorption at short-wavelengths. However, only combined radiation and conduction with relatively simple geometry (concentric, uniform glass rods) were considered.

The desire to improve productivity has motivated researchers to develop a 2D model that is more accurate for drawing of large-diameter preforms at high speeds. Among these, Lee and Jaluria [6] and Choudhury and Jaluria [7] assumed a free-surface profile in the calculation to solve for the velocity and temperature field. Using intermediate free-surface profiles, Choudhury et al. [8] solved the 2D stream-vorticity governing equations, where a small-diameter preform of 1.2576 cm drawn at a relatively slow speed of 3 m/s was considered. Xiao and Kaminski [9] attempted to solve the 2D conjugate problem of glass and gas flow with free interface using the commercial finite-element code FIDAP. They found it difficult to obtain convergence (that was sensitive to the deformation mesh) as the number of radiative macrosurfaces increased. More recently, Yin and Jaluria [10] and Cheng and Jaluria [11] investigated the effects of process parameters on high-speed fiber drawing (up to 20 m/s).

For drawing large-diameter preforms at high speeds, it was found that the computed glass temperatures were well above the glass melting point at the furnace exit. This may imply that the glass cools to form a solid fiber after leaving the furnace and thus, the actual diameter and speed of the glass at the furnace exit are essentially unknown. In order to address some of the abovemen-

---

tioned problems encountered in simulating the free-surface profile of melting glass in the furnace domain, we offer the following in this paper:

1. A complete 2D numerical model is presented for solving the neck-down shape of melting glass in the furnace domain, which does not require specifying a value to the glass speed. Instead, a Neumann boundary condition (NBC) at the furnace exit is assigned, where the velocity gradient can be more practically computed from the controlled draw tension. The model presented here can be applied to optimization of the high-speed draw process with large-diameter preforms.

2. This represents the first attempt to solve the RTE directly using DOM for the radiation intensities in the problem of predicting the neck-down shape of a fiber-draw process. The solution does not assume that the glass is optically thick and does not neglect the glass absorption at the short-wavelength band. More specifically, we extend our earlier work [5] to solve the full coupled 2D problem involving the combined radiation and conduction with viscous flow in the melting glass with an unknown free surface.

3. This paper introduces a robust and efficient computation scheme to solve for the free-surface flow in fiber-draw process based on the use of staggered grids. This staggered-grid scheme guarantees strict energy conservation and as a result, a much smaller grid number than those used in the previous studies is needed for a specified preform diameter. In addition, the explicit boundary condition of the pressure is not required at the free surface for this grid.

4. The numerical model presented here has been experimentally validated. Unlike previous studies [1] and [8], where comparisons were made against experimental data obtained for a small-diameter preform (1 cm) drawn at a slow speed (1 m/s), we compare our numerical prediction against an experimentally measured neck-down profile for a large preform of 9 cm in diameter drawn at a high speed of 25 m/s. As will be shown, both the numerical results and experimental data are in excellent agreement.

Fig. 1 Schematic of free-surface flow in the furnace and post-chamber

2 Analysis

Figure 1 shows the melting of a fused-silica glass rod (preform) with free surface inside the cylindrical furnace and the subsequent cooling inside a postchamber. The interest here is to solve for the geometry of the neck-down shape so that the glass radius at the furnace exit can be determined. For this purpose, a complete 2D model is developed for the furnace-draw process. The following assumptions are made in the formulation:

1. The system is axisymmetric and two-dimensional. Only the furnace domain is considered, where the furnace walls are gray and diffuse.

2. The glass flow is Newtonian and incompressible. The glass is semitransparent to radiation in the spectral range $0<\lambda<5$ μm and is almost opaque beyond 5 μm. The scattering of radiation can be neglected (Viskanta [12]). The glass refractive index is uniform and does not depend on temperature.

3. The inner and outer surfaces at the glass interface are treated as diffuse for the radiation reflection and transmission. This assumption is based on the fact that the surface of the melting preform may undergo wavy hydrodynamic instabilities with magnitude in the order-of-radiation wavelengths.

2.1 Fluid Dynamic Model. The 2D fluid dynamic governing equations for the glass flow, which include the continuity, Navier-Stokes, and energy equations, are given below in the cylindrical coordinates (r,z) system [13]:

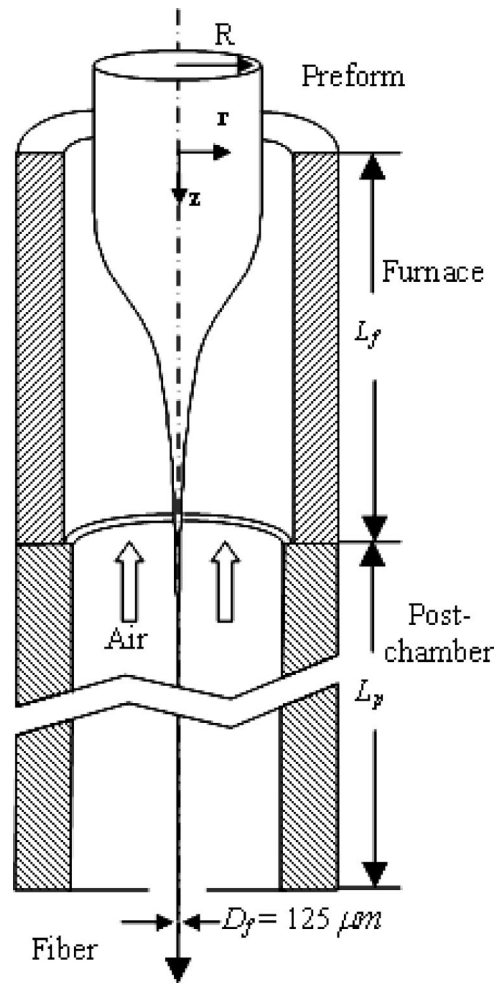$$\frac{1}{r}\frac{\partial}{\partial r}(r\rho u)+\frac{\partial}{\partial z}(\rho v)=0 \qquad (1)$$

$$\rho\frac{\partial u}{\partial t}+\rho u\frac{\partial u}{\partial r}+\rho v\frac{\partial u}{\partial z}=-\frac{\partial p}{\partial r}+\frac{1}{r}\frac{\partial}{\partial r}\left(2\mu r\frac{\partial u}{\partial r}\right)-2\mu\frac{u}{r^2}$$
$$+\frac{\partial}{\partial z}\left[\mu\left(\frac{\partial u}{\partial z}+\frac{\partial v}{\partial r}\right)\right] \qquad (2)$$

$$\rho\frac{\partial v}{\partial t}+\rho u\frac{\partial v}{\partial r}+\rho v\frac{\partial v}{\partial z}=-\frac{\partial p}{\partial z}+\frac{1}{r}\frac{\partial}{\partial r}\left[\mu r\left(\frac{\partial u}{\partial z}+\frac{\partial v}{\partial r}\right)\right]$$
$$+\frac{\partial}{\partial z}\left(2\mu\frac{\partial v}{\partial z}\right)+\rho g \qquad (3)$$

$$\rho C_p\left(\frac{\partial T}{\partial t}+u\frac{\partial T}{\partial r}+v\frac{\partial T}{\partial z}\right)=\frac{1}{r}\frac{\partial}{\partial r}\left(kr\frac{\partial T}{\partial r}\right)+\frac{\partial}{\partial z}\left(k\frac{\partial T}{\partial z}\right)$$
$$-\nabla\cdot\mathbf{q}_R+\mu\Phi \qquad (4)$$

where

$$\Phi=2\left[\left(\frac{\partial u}{\partial r}\right)^2+\left(\frac{u}{r}\right)^2+\left(\frac{\partial v}{\partial z}\right)^2\right]+\left(\frac{\partial u}{\partial z}+\frac{\partial v}{\partial r}\right)^2$$

and $\mathbf{q}_R$ is the radiation heat flux in the participating glass media, the solution of which will be described in Section 2.2. Other symbols in the above equations are defined in the Nomenclature.

The artificial compressibility method (ACM) [14] is used to solve the pressure-velocity coupled Navier-Stokes equations nu-

merically in the glass domain. An artificial time derivative of the pressure is added to the continuity equation as follows:

$$\frac{\partial p}{\partial \tilde{t}} + a\left[\frac{1}{r}\frac{\partial}{\partial r}(ru) + \frac{\partial v}{\partial z}\right] = 0 \qquad (5)$$

where $\tilde{t}$ is a fictitious time and a is the artificial compressibility factor.

The full 2D fluid dynamic model has five variables to solve; u, v, p, R, and T. The momentum and energy equations are strongly coupled because the viscosity of the glass changes by several orders of magnitude with temperature. Furthermore, the energy equation is highly nonlinear due to the radiative heat transfer between the furnace and the glass. The coupled equations (2)–(5) are solved numerically along with the following boundary conditions.

Since the system is axisymmetric, we have along the centerline or at

$$r = 0, \quad u = 0, \quad \frac{\partial v}{\partial r} = 0, \quad \frac{\partial T}{\partial r} = 0 \qquad (6)$$

At the furnace inlet or at

$$z = 0, \quad u = 0, \quad v = v_{in}, \quad \frac{\partial^2 T}{\partial z^2} = 0, \quad R = R_p \qquad (7)$$

where v_{in} is the feed rate and R_p is the preform radius. The glass temperature is extrapolated at the furnace inlet since no significant differences were found in the simulations even when a more detailed temperature boundary condition was modeled.

The boundary conditions at the free surface are as follows:

Normal force balance: $\quad p_g - p_a + \zeta\kappa = 2\mu_g\left.\frac{\partial V_n}{\partial n}\right|_g - 2\mu_a\left.\frac{\partial V_n}{\partial n}\right|_a$ (8)

Tangential force balance: $\quad \mu_g\left.\frac{\partial V_t}{\partial n}\right|_g = \mu_a\left.\frac{\partial V_t}{\partial n}\right|_a \approx 0 \qquad (9)$

Net heat flux continuity: $\quad -k_g\left.\frac{\partial T}{\partial n}\right|_g = q_{rad,opa} + q_{conv}$ (10)

Kinematic condition: $\quad \frac{\partial R}{\partial t} + v\frac{\partial R}{\partial z} - u = 0 \qquad (11)$

where ζ is the surface tension and κ is the surface curvature; V_n and V_t are the normal and tangential components of the velocity at the interface; n is the magnitude of the normal vector; $q_{rad,opa}$ is the net radiation heat flux in the opaque band; q_{conv} is the natural convection heat flux from the air; the subscripts g and a denote the glass and air, respectively; and R is the radius of the glass, which is a function of z. In Eq. (8), the surface tension and the normal stress of the air can be neglected because they are several orders smaller than the other terms; p_a is set to 0 as a reference. Equations (8)–(11) can be used as the boundary conditions for variables u, v, T, and $R(z)$, respectively.

At the furnace exit, the glass temperature is extrapolated, as the downstream temperature of the glass outside the furnace does not have considerable effect on the upstream temperature of the glass

$$\text{at } z = L_f, \quad \frac{\partial u}{\partial z} = 0, \quad \frac{\partial^2 T}{\partial z^2} = 0 \qquad (12)$$

In addition, we use the NBC for the axial velocity (instead of assuming an arbitrary value for the glass velocity at the furnace exit; often, the value of the specified fiber draw speed is used in published literature). The NBC can be obtained from the elongation model for the draw tension [1]:
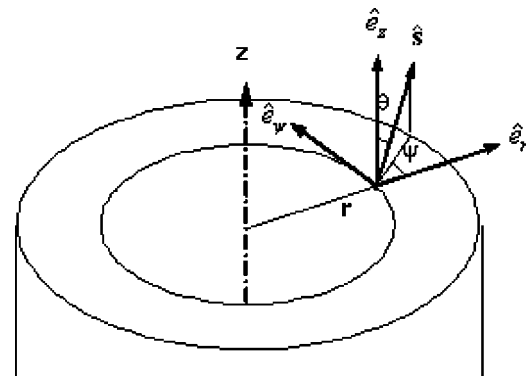
Fig. 2 Intensity orientation vector in the 2D axisymmetric cylindrical coordinates system

$$\text{at } z = L_f, \quad \frac{dv}{dz} = \frac{F_t}{3\mu\pi R_{L_f}^2} \qquad (13)$$

where F_t is the specified draw tension on the fiber. It is worth noting that the glass may not reach the specified diameter at the furnace exit; thus, the glass velocity at the furnace exit is often an unknown. On the other hand, the value of the draw tension F_t can be measured and controlled immediately after the postchamber. Because the glass diameter is very small after it exits the furnace, its inertia and gravitational effects between the furnace exit and the tension measuring point are negligible in Eq. (13). The glass radius at the furnace exit R_{L_f} is known once the free surface is determined.

2.2 Radiation Model. The energy equation requires the divergence of the radiation heat flux $\mathbf{q}_R$ that can be obtained by

$$\nabla \cdot \mathbf{q}_R = \int_0^\infty \left[4\pi\kappa_\lambda n_\lambda^2 I_{b\lambda}(T) - \kappa_\lambda \int_{\Omega = 4\pi} I_\lambda(\mathbf{r},\mathbf{s})d\Omega\right]d\lambda \quad (14)$$

where the spectral radiative intensity $I_\lambda(\mathbf{r},\mathbf{s})$ is a function of the position vector $\mathbf{r}$, orientation vector $\mathbf{s}$, and wavelength λ; $I_{b\lambda}(T)$ is the spectral intensity of a blackbody radiation given by Planck's function; κ_λ is the spectral absorption coefficient. The radiative intensity is obtained by solving the RTE:

$$\frac{\alpha}{r}\frac{\partial(rI_\lambda)}{\partial r} - \frac{1}{r}\frac{\partial(\gamma I_\lambda)}{\partial\psi} + \beta\frac{\partial I_\lambda}{\partial z} = \kappa_\lambda[I_{b\lambda}(T) - I_\lambda] \qquad (15)$$

where $(\alpha,\gamma,\beta) = (\sin\theta\cos\psi, \sin\theta\sin\psi, \cos\theta)$ describes the direction cosines of the orientation vector $\mathbf{s}$; and θ and ψ are defined in Fig. 2.

Due to the arbitrary change of the free interface, Eq. (15) is cast into the fully conservative form in a general curvilinear coordinate system (η,ξ)

$$\frac{\partial[rG(\alpha\eta_r + \beta\eta_z)I_\lambda]}{\partial\eta} + \frac{\partial[rG(\alpha\xi_r + \beta\xi_z)I_\lambda]}{\partial\xi} - G\frac{\partial(\gamma I_\lambda)}{\partial\psi}$$
$$= \kappa_\lambda rG[n_\lambda^2 I_{b\lambda}(T) - I_\lambda] \qquad (16)$$

where (η_r, η_z) and (ξ_r, ξ_z) are the grid metrics; and G is the *Jacobian* of the transformation.

Equation (16) is solved numerically with the following boundary conditions. Along the axis of the cylinder or at

$$r = 0 \quad I_\lambda = I_\lambda' \quad \text{for } \beta = \beta', \quad \alpha = -\alpha' \qquad (17)$$

Because the temperatures of the preform and the ambient outside the furnace are much lower than that within the furnace, we can neglect the intensities from the outside of the furnace

$$\text{at } z = 0, \quad I_\lambda \approx 0 \quad \text{for } \beta > 0 \qquad (18)$$

and

$$\text{at } z = L_f, \quad I_\lambda \approx 0 \quad \text{for } \beta < 0 \tag{19}$$

For a diffuse interface, the radiation intensity at the inner glass surface pointing inward is given by

$$I_\lambda(\mathbf{r},\mathbf{s}) = \frac{(1-\rho_\lambda^+)H_\lambda + \rho_\lambda^-(q_{\lambda,r}^+\mathbf{r} + q_{\lambda,z}^+\mathbf{z})\cdot\mathbf{n}}{\pi} \quad \mathbf{s}\cdot\mathbf{n}<0 \tag{20}$$

where ρ_λ^+ and ρ_λ^- are the reflectivities at the outer and inner surfaces, respectively; $q_{\lambda,r}^+$, $q_{\lambda,z}^+$ are the one-way spectral fluxes in the glass in the positive r and z directions, respectively; $\mathbf{n}$ is the unit normal vector at the free interface pointing outward; and H_λ is the irradiation on the outer surface.

In order to obtain the irradiation H_λ in Eq. (20), the radiosities of the furnace wall must be determined. For this, we consider the enclosure formed by the glass outer surface, the furnace wall, and the top and bottom disk openings. The radiosities on the glass outer surface are given by

$$J_\lambda = (1-\rho_\lambda^-)(q_{\lambda,r}^+\mathbf{r} + q_{\lambda,z}^+\mathbf{z})\cdot\mathbf{n} + \rho_\lambda^+ H_\lambda \quad 0<\lambda<5 \ \mu\text{m} \tag{21}$$

$$J_\lambda = \varepsilon E_{b\lambda} + (1-\varepsilon)H_\lambda \quad \lambda>5 \ \mu\text{m} \tag{22}$$

where ε is the emissivity of the surface, and $E_{b\lambda}$ is the blackbody emissive power. Since the furnace is opaque, its radiosities are also calculated from Eq. (22) in all the spectral range. The enclosure is divided into K small ring elements, and thus, the irradiations can be expressed as

$$H_{\lambda,i} = \sum_{j=1}^{K} J_{\lambda,j}F_{i-j} \tag{23}$$

where F_{i-j} is the diffuse view factor from surface element i to j. Substituting Eq. (23) into Eqs. (21) and (22) followed by applying the resulting equations on each surface element, a system of linear equations for the radiosities can be obtained. Once the radiosities are solved, the irradiations can be determined from Eq. (23). The formula derived by Myers [3] is used to calculate the view factors from the glass surface to the furnace wall. The view factor from one furnace element to another is obtained by numerical integration considering the block of the view by the preform.

In this study, the discrete ordinate method (DOM) is used to solve Eq. (16). A detailed procedure of the method and the absorption coefficient band model can be found in [5].

3 Numerical Method

The staggered grid [15] is used in solving for the free surface due to the following advantages:

1. The method guarantees the strict energy conservation in the finite volume discretization so that a smaller grid number can be used.
2. The fluctuations in the solution (especially at the free surface) due to the central differencing of the first derivative terms are avoided.
3. There is no need for the explicit boundary condition for pressure at the free surface.

The staggered grid scheme, though it requires tedious interpolations of variables, is robust and efficient.

Since the free interface has an arbitrary neck-down profile, the governing equations and boundary conditions are transformed into a curvilinear coordinates system (η,ξ). Second-order accurate finite differencing is applied to discretize the equations. The linear equations are in semi-implicit form, as the source term is evaluated at every previous time step. In solving the Navier-Stokes equations, the pressure in Eq. (5) is updated explicitly by an artificial time-marching scheme at each real time step. The pressure derivative term vanishes when this iteration converges so that the continuity equation is satisfied.

Implementation of the Free Surface Boundary Conditions. Using the following definitions for the normal and tangential velocity components at the free surface, Eqs. (8) and (9) are implemented using the staggered grid; appropriate discretization and manipulation are required to ensure stable and robust convergence in the computation

$$V_n = \mathbf{v}\cdot\mathbf{n} = u\frac{\eta_r}{\sqrt{g^{11}}} + v\frac{\eta_z}{\sqrt{g^{11}}} \tag{24}$$

$$V_t = \mathbf{v}\cdot\mathbf{t} = -u\frac{\eta_z}{\sqrt{g^{11}}} + v\frac{\eta_r}{\sqrt{g^{11}}} \tag{25}$$

where $\mathbf{n}=(n_r,n_z)^T$ and $\mathbf{t}=(t_r,t_z)^T$ are the unit vectors in the normal and tangential directions at the free surface; and the grid metric tensor $g^{11}=\eta_r^2+\eta_z^2$.

Substituting Eqs. (24) and (25) into Eqs. (8) and (9) and transforming them into the (η,ξ) coordinates, the following expressions can be derived:

$$\frac{2\mu}{\sqrt{g^{11}}}\left[g^{11}\frac{\partial}{\partial\eta}(n_r u + n_z v) + g^{12}\frac{\partial}{\partial\xi}(n_r u + n_z v) - B^n u - C^n v\right]$$
$$= p_g + \zeta\kappa \tag{26}$$

$$g^{11}\frac{\partial}{\partial\eta}(-n_z u + n_r v) + g^{12}\frac{\partial}{\partial\xi}(-n_z u + n_r v) + G\frac{\partial}{\partial\xi}(n_r u + n_z v)$$
$$- B^t u - C^t v = 0 \tag{27}$$

where

$$B^n = g^{11}\frac{\partial}{\partial\eta}(n_r) + g^{12}\frac{\partial}{\partial\xi}(n_r) \tag{28a}$$

$$C^n = g^{11}\frac{\partial}{\partial\eta}(n_z) + g^{12}\frac{\partial}{\partial\xi}(n_z) \tag{28b}$$

$$B^t = g^{11}\frac{\partial}{\partial\eta}(-n_z) + g^{12}\frac{\partial}{\partial\xi}(-n_z) + G\frac{\partial}{\partial\xi}(n_r) \tag{28c}$$

$$C^t = g^{11}\frac{\partial}{\partial\eta}(n_r) + g^{12}\frac{\partial}{\partial\xi}(n_r) + G\frac{\partial}{\partial\xi}(n_z) \tag{28d}$$

The grid metric tensor $g^{12}=\eta_r\xi_r + \eta_z\xi_z$ and the Jacobian $G = \eta_r\xi_z - \xi_r\eta_z$.

The first derivatives of the velocity components in Eqs. (26) and (27) must be evaluated along the free surface. We define u at the surface and v half a grid away from the boundary. In order to maintain the second-order accuracy in the differencing, the glass domain is extended outward by half a grid size, and a fictitious v component is defined on the new boundary as shown in Fig. 3 in dashed lines. The second-order accurate finite differencing can be implemented on the gray-colored control volume right on the free surface with the grid molecules shown in Fig. 3(a) as
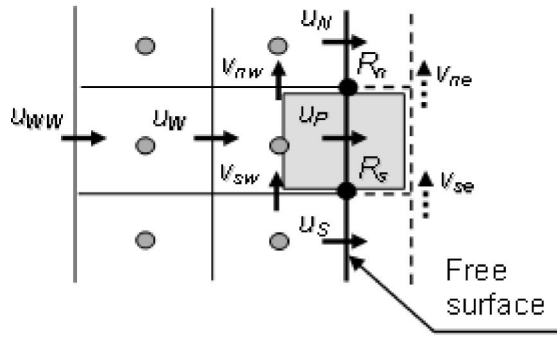
$$\frac{\partial u}{\partial\eta} = 1.5u_P - 2u_W + 0.5u_{WW} \tag{29a}$$

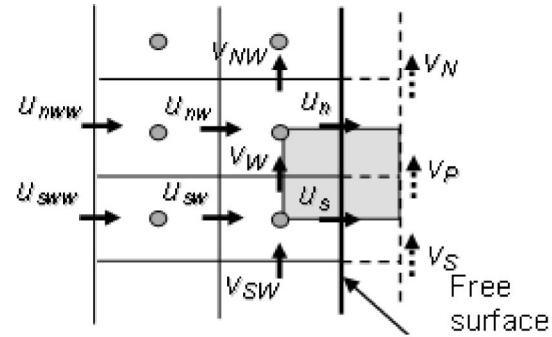$$\frac{\partial u}{\partial\xi} = 0.5(u_S - u_N) \tag{29b}$$

$$\frac{\partial v}{\partial\eta} = 0.5(v_{ne} + v_{se} - v_{nw} - v_{sw}) \tag{29c}$$

$$\frac{\partial v}{\partial\xi} = 0.5(v_{sw} + v_{se} - v_{nw} - v_{ne}) \tag{29d}$$

and with the grid molecules shown in Fig. 3(b) as

(a) control volume for *u* at the free surface (b) control volume for *v* at the free surface

Fig. 3 Grid molecules for the staggered grid at the free surface a) control volume for *u* at the free surface b) control volume for *v* at the free surface

$$\frac{\partial v}{\partial \eta} = (v_P - v_W) \tag{30a}$$

$$\frac{\partial v}{\partial \xi} = 0.25(v_{SW} + v_S - v_{NW} - v_N) \tag{30b}$$

$$\frac{\partial u}{\partial \eta} = 0.5(1.5u_n - 2u_{nw} + u_{nww} + 1.5u_s - 2u_{sw} + u_{sww}) \tag{30c}$$

$$\frac{\partial u}{\partial \xi} = (u_s - u_n) \tag{30d}$$

Equations (29) and (30) are substituted into Eqs. (26) and (27), respectively, and the resulting linear equations are used as the boundary conditions for the velocity components u_p and v_p, respectively.

For the temperature boundary condition in Eq. (10), the radiation flux in the opaque band can be obtained, after the radiosities are solved in the enclosure analysis, and is simply given by $q_{rad,opa} = J_{opa} - H_{opa}$. The natural convection heat flux q_{conv} can be calculated numerically from the natural convection of the air in the open-ended channel. It is necessary to include the postchamber along with a detailed boundary condition at the entrance.

The axial derivative of the radius in Eq. (11) can be discretized as $\partial R/\partial z = (R_s - R_n)/dz$, where the nodes for R_s and R_n are located between every two adjacent *u* components as shown in Fig. 3(a). In this way, R_s and R_n are adjacent and the numerical fluctuations due to the central differencing using every other two nodes are avoided. The v component in Eq. (11) can be interpolated at the location of u_P using the adjacent four component values.

Computation Scheme. The free surface and the velocity and temperature fields are solved using the following procedures:

Step 1: Input the initial free surface profile and the values of the primitive variables (p, u, v, T).

Step 2: Temperature iteration (with a given free surface and the velocity field).

  a. Calculate the view factors.
  b. Solve Eq. (16) iteratively to solve for the intensities at the free interface.
  c. Then calculate $\nabla \cdot \mathbf{q}_R$ using Eq. (14).
  d. Solve the energy equation using implicit time marching scheme.
  e. Repeat Step 2a until a steady state is reached.

Step 3: Free surface inner iteration (the temperature field is fixed):

  a. Solve the Navier Stokes equations using ACM time marching scheme.
  b. Update free surface profile using kinematic condition, Eq. (11).
  c. Regenerate the curvilinear grid.
  d. Repeat Step 3a until a steady state has been reached.

Step 4: Free surface outer iteration

  a. Save the free surface profile obtained in Step 3.
  b. Compare it with the last result saved in Step 4.
  c. If the relative change between two consecutive computed free surface profiles is less than 10^{-5}, the final result is obtained; otherwise go back to Step 2.

As shown in the above procedures, the degrees of freedom (unknown variables) during the computation are effectively reduced by separating the temperature iteration and the free surface iteration. This results in a more robust and faster convergence in the computation.

4 Results and Discussions

A MATLAB program with C++ subroutines was written to simulate the free surface of a draw process. Numerical results were obtained for two geometries, where the values of the parameters are shown in Table 1. Case 1 was selected for validating the computational model. Case 2 was designed to study the effect of preform diameter on the computational model for a specified fiber diameter, draw speed, and tension on the fiber.

In both cases, the physical properties of the fused silica are taken from Fleming [16] and the three-band absorption coefficient model for the RTE can be found in [5]. Since the glass surface velocity is small and the air temperature is close to the glass temperature in the furnace domain, the convective heat flux is much smaller than the radiation flux. Hence the use of an approximate heat transfer coefficient h should not affect the accuracy of

Table 1 Parameters used in the simulation

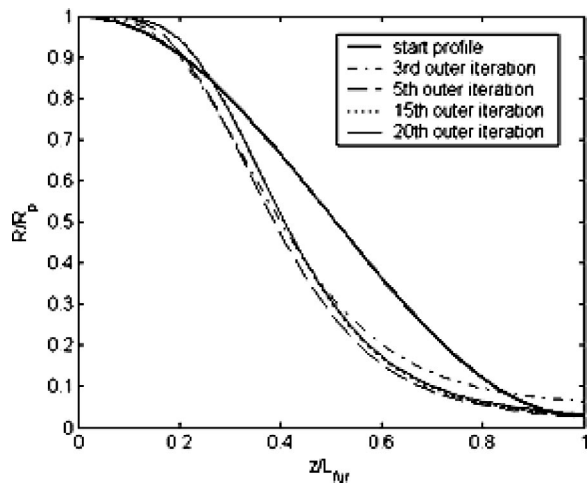| Parameters	Case 1	Case 2
Specified fiber diameter, R_f (μm)	62.5	
Specified draw speed, v_f (m/s)	25	
Specified draw tension, F_t (grams)	110	
Preform radius, R_p (m)	0.045	0.09
Furnace peak temperature, $T_{f,max}$ (K)	2,400	2,460
Furnace minimum temperature, $T_{f,min}$ (K)	1,700	1,760
Furnace radius, R_{fur} (m)	0.06	0.12
Furnace length, L_{fur} (m)	0.45	0.7

Fig. 4 Intermediate free-surface profiles during the outer iteration

(a) Neck-down profiles

(b) Centerline temperatures

Fig. 5 Comparison of results (Case 1) (a) Neck-down profiles (b) Centerline temperatures
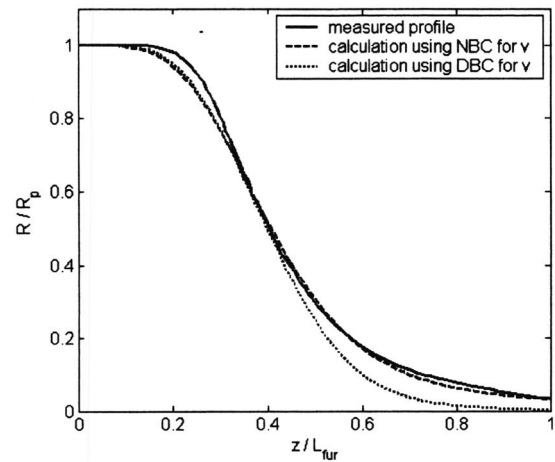
the solution significantly; however, the computation can be greatly reduced. A sinusoidal variation of h varying from 30 W/m^2 K at the furnace inlet to 50 W/m^2 K at the exit was used. This h was based on the combination of the experimental data in Paek [1] and simulation data from Yin and Jaluria [10]. The average air temperature inside the furnace was estimated to be 1900 K.

The numerical model developed here has the advantage of fast convergence. A nonuniform grid is used with a denser spacing near the interface. A grid-size study showed no noticeable changes in the results when the grid number is larger than 81×15 (in z and r directions, respectively). This is much smaller than 401×21 used by Choudhury et al. [8]. One of the reasons for the efficiency is that the staggered grid guarantees strict energy conservation in the finite volume discretizaiton and reduces fluctuations in the solution. It usually takes about 300 outer iterations to arrive at the final results; this means 2.5 h of computation with a desktop PC (AMD1700 CPU with a 512M RAM). If a less strict convergent criterion is used (say, from 10^{-5} to 10^{-3}), it only takes 40 outer iterations (or 45 min). However, the temperature iteration usually converges within 150 steps (or the relative change between two steps is less than 10^{-5}). The inner free-surface iteration in Step 3 may take as much as 4000 steps to reach a relative error residual of 10^{-4}. Since the temperature data is only intermediate, a maximum iteration limit of 1500 steps can be set in the inner iteration to reduce computational time.
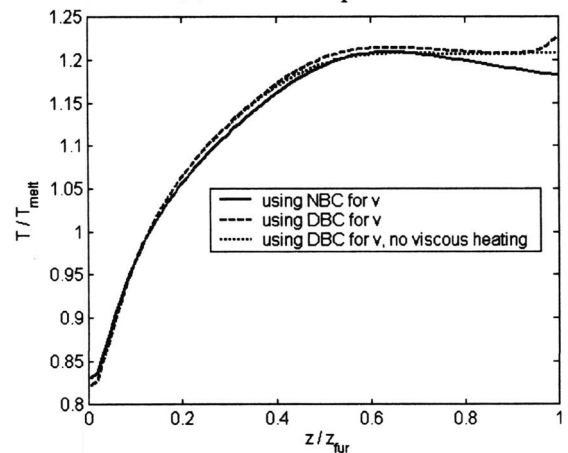
4.1 Simulation Case 1. The values for Case 1 were data provided by OFS so that models and numerical results can be validated experimentally. Thus, the temperature distribution of the furnace wall was experimentally measured [17] using a M90R single-color infrared thermometer (MIKRON, Inc.), which measures the radiosities at 0.65 μm wavelength. This was followed by a radiation analysis on the enclosure to obtain the emission intensities and consequently, the temperature of the furnace wall. The temperature distribution is parabolic with the maximum at the middle and minimum at both ends.

Figure 4 shows some intermediate free surface profiles during the outer iteration. It is noticed that the free surface profile converges very fast. There is not noticeable change in most part of the neck-down region after the 15th iteration. The diameter of the glass at the exit may vary during the iteration due to the Neumann boundary condition used for v.

Model Validation. The steady-state surface profile of the glass rod was experimentally measured for the purpose of validating the model. The preform was moved out of the furnace in a very short time (less than 1 min) to prevent shape deformation due to the
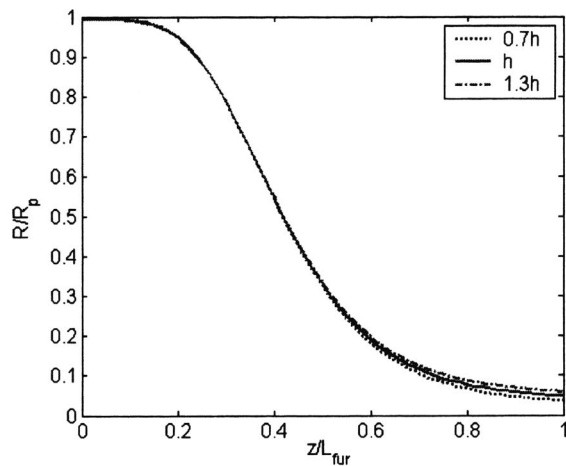
change of view factors. The handle of the preform was then held by a fixture and moved vertically at a constant speed while its diameter was measured by a laser scanner.

Figures 5(a) and 5(b) compare the free-surface profiles and the axial temperature distributions of the glass computed using two different boundary conditions at the furnace exit:
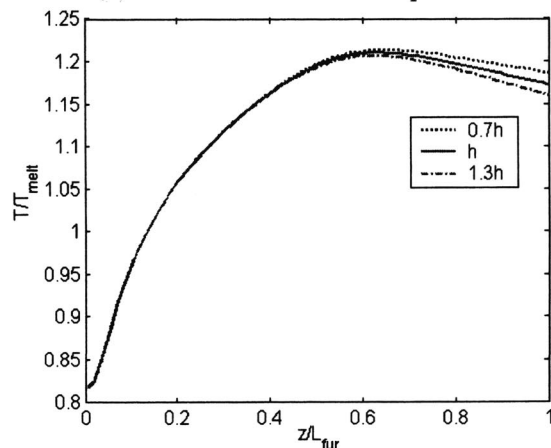
1. Neumann boundary condition (NBC) or Eq. (9), as proposed in this paper, which specifies the derivative of the glass exit velocity by computing it from the draw tension: $dv/dz = F_t/(3\mu\pi R_{L_f}^2)$.

2. Dirichlet boundary condition (DBC), commonly used, which assumes the draw speed as the glass velocity at the furnace exit: $v = v_f$.

The sensitivity of the free-surface profile and the axial temperature distributions to the changes of the heat transfer coefficient h (±30%) is illustrated in Figs. 6(a) and 6(b). The radial temperature distribution is given in Fig. 7.

Figure 5(a) compared the computed neck-down shape against the measured profile, where those predicted with NBC as suggested in this study is in excellent agreement with the experimental measurement. Those calculated using the DBC deviate significantly from the measurement, particularly near the furnace exit where the glass was assumed to move at the specified draw speed (or equivalently, the specified diameter at the exit). As compared in Fig. 5(b) where the temperature is normalized to the melting point of 1853 K, we note that the glass temperature increases

(a) Effect of h on neck-down profiles

(b) Effect of h on centerline temperatures

Fig. 6 Effects of heat transfer coefficient h (a) Effect of h on neck-down profiles (b) Effect of h on centerline temperatures

dramatically near the furnace exit in the case of DBC and as a matter of fact, reheating occurs and keeps it well above the glass melting point. The drastic increase in the glass temperature has been traced to the viscous heating induced by the unrealistic high-axial velocity gradient as the glass diameter converges rapidly to the assumed fiber diameter. This phenomenon is clearly in conflict with the assumption that the glass moving at the draw speed is a solid fiber having the desired (constant) diameter at the furnace
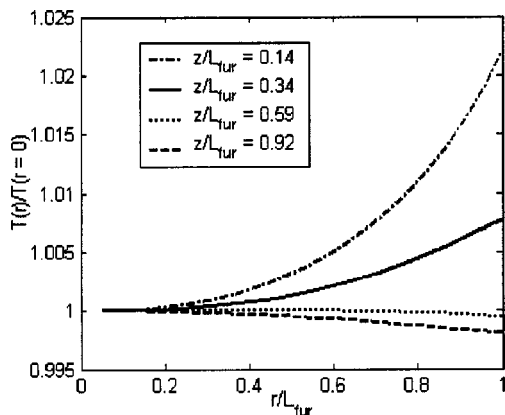

Fig. 7 Radial temperature distributions

exit. Hence, we conclude that the DBC is invalid for drawing large preforms at high speeds, where the fiber freezes well outside the furnace domain. Alternatively, draw tension can be utilized to obtain an appropriate NBC for specifying the derivative of the glass velocity in Eq. (13). NBC is thus used in the rest of the simulations.

As shown in Fig. 6, the solution is insensitive to the changes in h except near the furnace exit where the air convection becomes more pronounced. Figure 7 shows that the glass absorbs heat flux near the furnace inlet and dissipates heat flux at the furnace exit.

2-D Glass Flow. The glass flow of a large preform exhibits 2D characteristics that are not predicted with a 1D model. In order to provide a better understanding of the effects of the 2D velocity variation on the glass flow, a program utilizing the computed 2D velocity field was written.

Figure 8 shows the distributions of the radial and axial velocity components. Figure 8(a) shows an interesting radial variation of the glass axial velocity v. Near the furnace inlet, the glass melts from the surface due to the positive radial temperature gradient (Fig. 7) while it remains largely solid at the center. Hence, the surface velocity is higher than the centerline velocity. The glass completely melts in the neck-down region (at about 1/3 L_f), the surface velocity becomes much slower than the centerline velocity. The radial variation of the axial velocity is small near the furnace exit where the molten glass is highly viscous and has a very small diameter. Figure 8(b) shows that the glass velocity increases exponentially in the neck-down region. Figure 8(c) shows that the radial velocity u is linear with r near the furnace exit, which is governed by the continuity equation with the almost 1D distribution of v. In the neck-down region, the distribution of u is nonlinear due to the radial variation of v.

The visualization program tracks a group of fictitious infinitesimal particles originally distributed at the same cross-section plane in the preform as they travel through the neck-down region. Snapshots of the particles can be graphed from the following integral:

$$\mathbf{r}(t) = \mathbf{r}(0) + \int_0^t \mathbf{V}[\mathbf{r}(s)]ds \tag{31}$$

where the location vector $\mathbf{r}$ is obtained by integrating the velocity vector $\mathbf{V}$ along a path in the r-z coordinate system; and s is a dummy integration variable representing time. Figure 9 shows how the particles travel through the neck-down region from the furnace inlet (or at $z=0$), where the dashed lines represent the interface between the core rod and the cladding tube. As predicted in Fig. 9(a), the particle distributions become dramatically distorted once they move past 1/3 of the furnace length where the glass axial velocity is faster in the center than that near the surface. Although the radial variation of the axial velocity is small, it causes a distortion of the particle distribution due to the exponential increase in the axial velocity in the z direction as shown in Fig. 8(b). Simple 1D models are not able to capture this 2D particle flow pattern. This visualization could be used to track the change in the gap geometry, which occurs between two stacked cores in the glass preform. The study, however, requires extending the computation domain to the solidification of the fiber and is beyond the scope of this paper.

4.2 Simulation Case 2. The effects of a large-diameter preform on the computational model were studied using Case 2. Two numerical updating-schemes are compared, where the furnace temperature and geometry were modified appropriately to accommodate the large preform and to keep a reasonable furnace length.

1. Semi 2D solution using radially lumped 1D axial velocity and mass conservation [8].
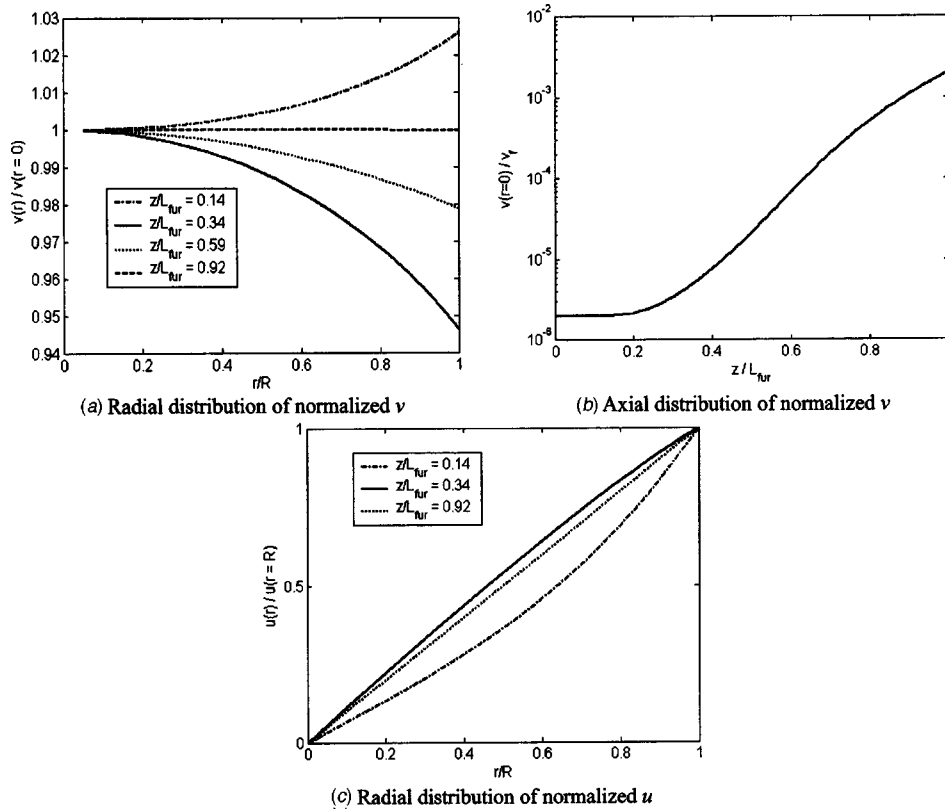
Fig. 8 Velocity distributions of the preform (*a*) Radial distribution of normalized *v* (*b*) Axial distribution of normalized *v* (*c*) Radial distribution of normalized *u*

2. Complete 2D solution using kinematic boundary condition in Eq. (11).

Comparisons are shown in Figs. 10(*a*) to 10(*c*). As shown in Fig. 10(*a*), the diameter of the preform in the neck-down region predicted by the semi-2D model is smaller than that from the 2D model. Consequently, the temperature in that region is higher due to the higher view factors to the hot spot of the furnace. At the bottom of the furnace, the diameter of the glass from the semi-2D model is larger than that in the full 2D model. As a consequence,

the velocity of the glass is smaller, as shown in Fig. 10(*b*), since the mass flow rate is conserved in the axial direction. The axial mass advection is weaker as the velocity is smaller, which results in a lower temperature near the exit in the semi-2D solution as shown in Fig. 10(*c*). It can be expected that the difference will be significant for the prediction of the location where the glass turns into fiber if the postchamber is included in the computation domain. This prediction is important for the industry to determine the necessary length of the postchamber.
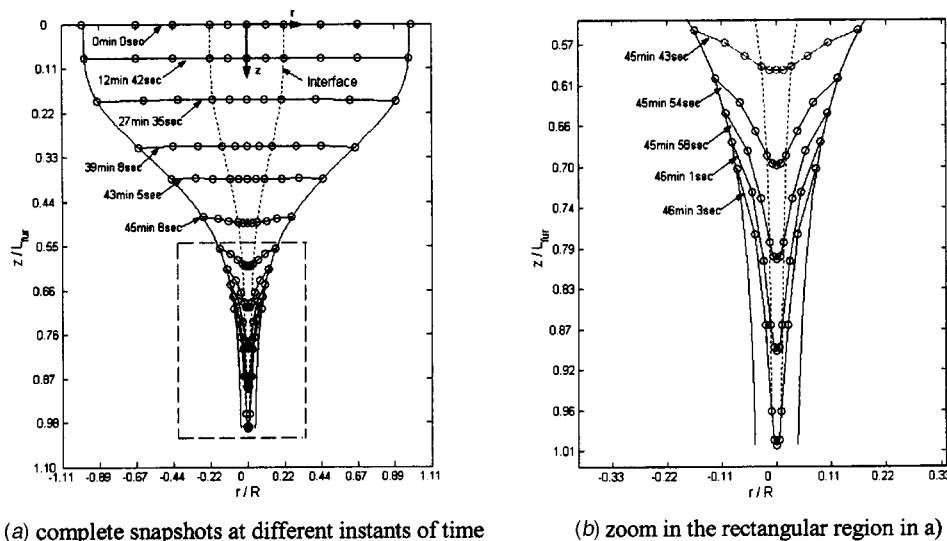

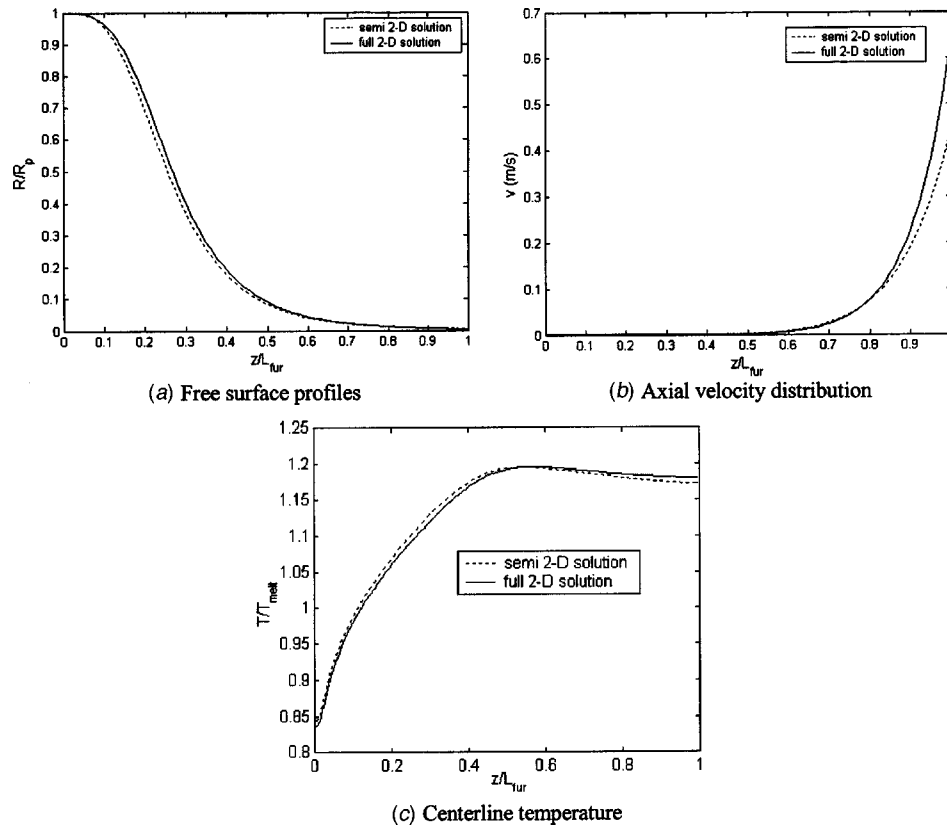**Fig. 9 Particle flow tracking *a*) complete snapshots at different instants of time *b*) zoom in the rectangular region in a)**

Fig. 10 Comparisons between semi-2D and full 2D models (*a*) Free surface profiles (*b*) Axial velocity distribution (*c*) Centerline temperature

5 Conclusions

A complete 2D numerical model for the high-speed fiber-drawing process in the furnace domain has been presented. This model uses the controlled draw tension to calculate the Neumann boundary condition at the furnace exit, and thus, it does not require specifying an assumed value to the glass speed as most previous studies did. The RTE has been directly solved for the radiation intensities using DOM, which is coupled with the solution of the free-surface flow. The computation scheme is shown to be efficient and robust. The required grid number is much smaller than that used in the previous study although the preform is larger and the furnace is longer.

The predicted free surface with NBC has been experimentally validated. The experimentally measured profile well agrees with that derived numerically. We have also noted that the free surface calculated using the DBC deviates significantly from the measured profile, particularly near the furnace exit. As the glass cools to form solid fiber after leaving the furnace, the actual diameter (and, hence, the speed) of the glass at the furnace exit is essentially unknown. This implies that assigning an arbitrary value to the glass speed at the furnace exit may not be valid for drawing large preforms at high speed.

The effects of the preform diameter on the free-surface calculation with a draw speed of 25 m/s have also been examined. Comparisons between the full and semi-2D models show that the difference is considerable when the preform has a large diameter. This difference is particularly significant if the interest is to predict the location where the glass converges to form the fiber of 125 μm in diameter. Our next step is to extend the computation domain to include the postchamber, and the conjugate problem of the glass flow and the natural convection of the air in the chamber will be solved.

Acknowledgments

Nomenclature

C_p = Specific heat
$E_{b\lambda}$ = blackbody emissive power
F_{i-j} = diffuse view factor from element i to element j
F_t = draw tension
G = Jacobian of the grid transformation
H_λ = irradiation
I_λ = spectral radiative intensity
$I_{b\lambda}$ = spectral blackbody intensity
J_λ = spectral radiosity
L_f = furnace length
R = glass radius
R_f = fiber radius
R_{L_f} = glass radius at the furnace exit
R_p = preform radius
T = temperature
V_n, V_t = normal and tangential components of the velocity at the free surface
a = artificial compressibility factor
g = gravitational acceleration
g^{11}, g^{12} = grid metric tensors
k = thermal conductivity
n = magnitude of the normal vector
$\mathbf{n}$ = unit normal vector
p = pressure
$\mathbf{q}_R$ = radiation heat flux

$q_{rad,opa}$ = net radiation heat flux in the opaque band
q_{conv} = natural convection heat flux from the air
$q_{\lambda,r}^+, q_{\lambda,z}^+$ = one-way spectral radiative fluxes in the positive r and z directions
r = radial coordinate
$\mathbf{r}$ = position vector
$\mathbf{s}$ = orientation vector
$\tilde{t}$ = fictitious time
u = radial component of velocity
v = axial component of velocity
v_{in} = preform feed rate
v_f = fiber draw speed
z = axial coordinate
$\mathbf{k}_\lambda$ = spectral absorption coefficient
α, γ, β = direction cosines of the intensity orientation vector $\mathbf{s}$
θ = local polar angle
$\eta_r, \eta_z, \xi_r, \xi_z$ = grid metrics of the tranformation
$\rho_\lambda^+, \rho_{\bar{\lambda}}^+$ = reflectivities at the outer and inner surfaces, respectively
ε = emissivity
ρ = density
μ = dynamic viscosity
Φ = dissipation function
ζ = surface tension
κ = surface curvature
λ = wavelength
η, ξ = general curvilinear coordinates
ψ = local azimuthal angle

References

[1] Paek, U. C., and Runk, R. B., 1978, "Physical Behavior of the Neck-Down Region During Furnace Drawing of Silica Fibers," J. Appl. Phys., **49**, pp. 4417–4422.

[2] Homsy, G. M., and Walker, K., 1979, "Heat Transfer in Laser Drawing of Optical Fibers," Glass Technol., **20**(1), pp. 20–26.

[3] Myers, M. R., 1989, "A Model for Unsteady Analysis of Preform Drawing," AIChE J., **35**(4), pp. 592–602.

[4] Vasiljev, V. N., Dulnev, G. N., and Naumchic, V. D., 1989, "The Flow of a Highly Viscous Liquid With a Free Surface," Glass Technol., **30**(2), pp. 83–90.

[5] Wei, Z., and Lee, K. M., 2003, "Effects of Radiative Transfer Modeling on Transient Temperature Distribution in Semitransparent Glass Rod," ASME J. Heat Transfer, **125**, pp. 1–7.

[6] Lee, S. H.-K., and Jaluria, Y., 1997, "Simulation of the Transport Processes in the Neck-Down Region of a Furnace Drawn Optical Fiber," Int. J. Heat Mass Transfer, **40**, pp. 843–856.

[7] Choudhury, S. R., and Jaluria, Y., 1998, "Thermal Transport Due to Material and Gas Flow in a Furnace for Drawing an Optical Fiber," J. Mater. Res., **13**(2), pp. 494–503.

[8] Choudhury, S. R., Jaluria, Y., and Lee, S. H.-K., 1999, "A Computational Method for Generating the Free-Surface Neck-Down Profile for Glass Flow in Optical Fiber Drawing," Numer. Heat Transfer, Part A, **35**, pp. 1–24.

[9] Xiao, Z., and Kaminski, D. A., 1997, "Flow, Heat Transfer, and Free Surface Shape During the Optical Fiber Drawing Process," *HTD Vol. 347, National Heat Transfer Conference*, ASME, New York, Vol. 9, pp. 219–229.

[10] Yin, Z., and Jaluria, Y., 2000, "Neck Down and Thermally Induced Defects in High-Speed Optical Fiber Drawing," ASME J. Heat Transfer, **122**, pp. 351–362.

[11] Cheng, X., and Jaluria, Y., 2002, "Effect of Draw Furnace Geometry on High-Speed Optical Fiber Manufacturing," Numer. Heat Transfer, Part A, **41**, pp. 757–781.

[12] Viskanta, R., and Anderson, E. E., 1975, "Heat Transfer in Semitransparent Solids," Adv. Heat Transfer, **11**, pp. 317–441.

[13] Schlichting, H., and Gersten, K., 1999, *Boundary Layer Theory*, Springer, Berlin.

[14] Chorin, A. J., 1967, "A Numerical Method for Solving Incompressible Viscous Flow Problems," J. Comput. Phys. **2**, pp. 12–26.

[15] Patankar, S. V., 1980, *Numerical Heat Transfer and Fluid Flow*, Hemisphere Publishing, Washington, DC.

[16] Fleming, J. D., 1964, "Fused Silica Manual," Final Report for the U.S. Atomic Energy Commission, Oak Ridge, Tennessee, Project No. B-153.

[17] Garner, H., 2000, "An Experimental Procedure for Measuring Furnace Temperature Profiles in Optical Fiber Drawing," Lucent Technologies internal report.